Structural, electronic, magnetic, and transport properties of the equiatomic quaternary Heusler alloy CoRhMnGe: Theory and experiment

Deepika Rani,[1] Enamullah,[1] K. G. Suresh,[1] A. K. Yadav,[2] S. N. Jha,[2] D. Bhattacharyya,[2] Manoj Raama Varma,[3] and Aftab Alam[1,*]

[1]*Department of Physics, Indian Institute of Technology Bombay, Powai, Mumbai 400076, Maharashtra, India*
[2]*Atomic and Molecular Physics Division, Bhabha Atomic Research center, Mumbai-400094, India*
[3]*National Institute for Interdisciplinary Sciences and Technology (CSIR), Thiruvananthpuram, India*

(Received 7 June 2017; revised manuscript received 24 October 2017; published 6 November 2017)

In this work, we present structural, electronic, magnetic, mechanical, and transport properties of equiatomic quaternary Heusler alloy, CoRhMnGe, using theoretical and experimental techniques. A detailed structural analysis is performed using x-ray diffraction and extended x-ray absorption fine structure spectroscopy. The alloy is found to crystallize in Y-type structure having space group $F\bar{4}3m$ (no. 216). The *ab initio* simulation predicts half-metallic ferromagnetic characteristics leading to large spin polarization. The calculated magnetization is found to be in fair agreement with experiment as well as those predicted by the Slater-Pauling rule, which is a prerequisite for half-metallicity. The magnetic transition temperature (T_C) is found to be ∼760 K. Measured electrical resistivity in the temperature range 2–400 K also gives an indication of half-metallic behavior. Effect of hydrostatic pressure on electronic structure, magnetic, and mechanical properties are investigated in detail. The alloy is found to preserve half-metallic characteristics up to 30.27 GPa, beyond which it transits to metallic phase. No magnetic phase transition is found to occur in the whole range of pressure. The system also satisfies the Born-Huang criteria for mechanical stability up to a limited range of pressure. All these properties make the CoRhMnGe alloy promising for spintronics devices.

DOI: 10.1103/PhysRevB.96.184404

I. INTRODUCTION

In the past few years, spintronics has emerged as a new field of research, utilizing spin currents, instead of electrons, as one of mediator for transport. It has proved to be quite promising for new types of fast electronic devices over conventional electrical charge-based semiconductor devices with advantages of high storage density, increased data processing speed, and low power consumption [1]. To enhance the efficiency of spintronic devices, the carrier for the concerned materials should be fully spin polarized. Half-metallic ferromagnets (HMFs) are great sources for highly spin polarized current and thus are ideal materials for spintronic based applications. Half-metallicity is found in magnetic materials in which one of the spin-polarized subband has a band gap and the other exchange-split subband has a nonzero density of states at the Fermi level (E_F); thus in these materials the electrical conduction takes place from one spin channel exclusively. The discovery of half-metallicity in half-Heusler alloy NiMnSb [2], by de Groot *et al.* in 1983, has intensified the interest in Heusler alloys for applications in the field of spintronics. The Heusler family of compounds are usually of two types: (i) a ternary material with stoichiometry 1:1:1 known as half-Heusler compounds (XYZ) and (ii) also a ternary material but with stoichiometry 2:1:1 known as full-Heusler compounds (X_2YZ). There is another class of Heusler compounds which have been discovered recently with stoichiometry 1:1:1:1, and are known as equiatomic quaternary Heusler alloys ($XX'YZ$), where X, X', and Y are transition metals and Z is a main group element [3]. The half-Heusler alloys crystallize in $C1_b$ structure (space group no. 216, $F\bar{4}3m$) with prototype MgAgAs and the full Heusler alloys crystallize in the cubic space group $Fm\bar{3}m$ (no. 225), with Cu_2MnAl ($L2_1$) as prototype, whereas the quaternary Heusler alloys crystallize in cubic space group (no. 216) with LiMgPdSn as prototype (Y type) [4]. Among the full Heusler compounds, considerable attention has been paid to the Co based compounds because of their high spin polarization and high Curie temperature [1,5–8], which make them more suitable for applications in spintronics. According to the Jullière model [9], the high spin polarization is very advantageous for getting high tunneling magnetoresistance ratios in magnetic tunnel junctions. The quaternary Heusler alloys CoRhMnZ (Z = Ga, Sn, and Sb) have been studied in detail by both theoretical and experimental methods and were found to be HMF by *ab initio* calculations [10]. CoRhMnGe, however, has not been studied from an experimental front. Hence keeping in view the increased interest and applications of Co-based Heusler alloys, we present a comprehensive study of electronic, structural, magnetic, and transport properties of CoRhMnGe (CRMG) Heusler alloy.

CRMG alloy is found to exist in the ordered cubic Heusler structure (Y type) with space group $F\bar{4}3m$ (no. 216). We have done a detailed local structure analysis using extended x-ray absorption fine structure (EXAFS) spectroscopy. The saturation magnetization value M_s at 5 K is found to be 4.9 μ_B/f.u., which is in close agreement with the value predicted by the Slater-Pauling rule (5 μ_B/f.u.) for half-metallic materials. The Curie temperature (T_C) was found to be ∼760 K, which is highest among the reported CoRhMnZ (Z = Ga, Sn, Sb) alloys [10]. We have also performed systematic *ab initio* calculations to study the electronic structure, magnetism and mechanical properties of the alloy. *Ab initio* simulations also predict a half-metallic nature for this alloy. Total energy and lattice dynamics calculations suggest that the alloy is

*aftab@iitb.ac.in

chemically and mechanically stable against external pressure. Effect of pressure on magnetism and half-metallicity is studied at length.

II. EXPERIMENTAL DETAILS

A. Sample synthesis

The polycrystalline alloy CRMG was prepared by arc melting the stoichiometric amounts of constituent elements (at least 99.9% purity) in water cooled copper hearth under high purity argon atmosphere. To further reduce the contamination a Ti ingot was used as an oxygen getter. 2% extra Mn was taken to compensate the weight loss due to Mn evaporation during melting. The ingot formed was flipped and melted several times for better homogeneity. The final weight loss was less than 1%.

B. Characterization

X-ray diffraction (XRD) pattern was taken at room temperature using Xpert pro diffractometer with Cu $K\alpha$ radiation to study the crystal structure of the sample. XRD analysis was done with the help of FullProf suite which uses the least square refinement between the experimental and calculated intensities. The Rietveld method is used to optimize the χ-square function given by

$$\chi^2 = w_i \Sigma_i (y_{\text{iobs}} - y_{\text{ical}})^2, \quad (1)$$

where w_i is the inverse of the variance associated with the ith observation, i.e., $\sigma^2(y_{\text{iobs}})$ and y_{iobs} and y_{ical} are the observed and calculated scattering intensities for a diffraction angle $2\theta_i$ [11]. It also contains the GFourier program, which is used to calculate and visualize the electron density within the unit cell.

EXAFS (extended x-ray absorption fine structure) measurements on CRMG were done to probe the local structure surrounding the Co, Ge, and Mn sites. The x-ray absorption spectroscopy (XAS) measurements have been carried out at the energy-scanning EXAFS beamline (BL-9) in transmission mode at the INDUS-2 Synchrotron Source (2.5 GeV, 200 mA) at Raja Ramanna Centre for Advanced Technology (RRCAT), Indore, India [12,13]. This beam-line operates in the energy range of 4–25 keV. The beamline optics consist of a Rh/Pt coated collimating meridional cylindrical mirror and the collimated beam reflected by the mirror is monochromatized by a Si(111) ($2d = 6.2709$ Å) based double crystal monochromator (DCM). The second crystal of the DCM is a sagittal cylinder used for horizontal focusing while a Rh/Pt coated bendable post mirror facing down is used for vertical focusing of the beam at the sample position. Three ionization chambers (300 mm length each) were used for data collection in the transmission mode; one for measuring incident flux (I_0), one for measuring transmitted flux (I_T), and the third for measuring EXAFS spectrum of a reference metal foil for energy calibration. Appropriate gas pressure and gas mixture have been chosen to achieve 10%–20% absorption in the first ionization chamber and 70%–90% absorption in second one to improve the signal to noise ratio. Rejection of the higher harmonics content in the x-ray beam was performed by the second mirror. The absorption coefficient, μ was obtained using the relation:

$$I_T = I_0 e^{-\mu x}, \quad (2)$$

where x is the thickness of the absorber. Powder samples of appropriate weight, estimated to obtain a reasonable edge jump, were taken and mixed thoroughly with cellulose powder to obtain total weight of 100 mg. Subsequently, homogeneous pellets of 15 mm diameter were prepared using an electrically operated hydraulic press. However, the grain size of the particles was of the order of 50 micron, which resulted in very bad data. The sample was later grounded continuously using a mortar-pestle for 3 h to reduce the particle size to less than 4 microns. This fine powder was dispersed on the scotch tape and larger particles are brushed out. A reasonable edge jump was obtained by folding the scotch tape.

Magnetization isotherms at 5 K and 300 K were obtained using a vibrating sample magnetometer (VSM) attached to the physical property measurement system (PPMS) (Quantum design) for fields up to 50 kOe. Thermomagnetic curves in the high temperature region (300–1000 K) were taken in VSM with attached high temperature oven under a field of 100 Oe. Electrical resistivity measurements were done using the four-probe method in PPMS.

III. COMPUTATIONAL DETAILS

Ab initio calculations were performed to study the electronic structure, magnetic, and mechanical properties using density functional theory (DFT) implemented within the Vienna *ab initio* simulation package (VASP) [14] with a projected augmented wave (PAW) basis [15]. The electronic exchange-correlation potential due to Perdew, Burke, and Ernzerhof (PBE) is used within the generalized gradient approximation (GGA) scheme. A 24^3 **k** mesh is used to perform the Brillouin zone integration within the tetrahedron method. A plane wave energy cutoff of 269 eV is used for all the calculations. All the structures are fully relaxed (cell volume, shape, and atomic positions of constituent atoms), with total energies (forces) converged to values less than 10^{-6} eV (0.01 eV/Å).

IV. RESULTS AND DISCUSSION

A. Structural stability

Quaternary Heusler alloys exhibit LiMgPdSn-type crystal structure whose primitive cell contains four atoms at the Wyckoff positions, $4a(0, 0, 0)$, $4b(1/2, 1/2, 1/2)$, $4c(1/4, 1/4, 1/4)$, and $4d(3/4, 3/4, 3/4)$. The preferred occupation depends upon the electronegativities and sizes of individual atoms. Hence we have calculated the total energies corresponding to different atomic configurations. We have found three non-degenerate atomic configurations, obtained by interchanging constituent atoms at various Wyckoff positions such as Type1, Type2, and Type3 with decreasing stability. The energetics and corresponding configurations are shown in Fig. 1. The most stable configuration (Type1) corresponds to the occupation: Co at $4d$, Rh at $4c$, Mn at $4b$, and Ge at $4a$ Wyckoff sites, which is also confirmed by the experiment (see x-ray diffraction subsection). On the other hand, in Type2 configuration, Co sits at $4b$, Rh at $4d$, Mn at $4c$, and Ge at $4a$ sites. The least

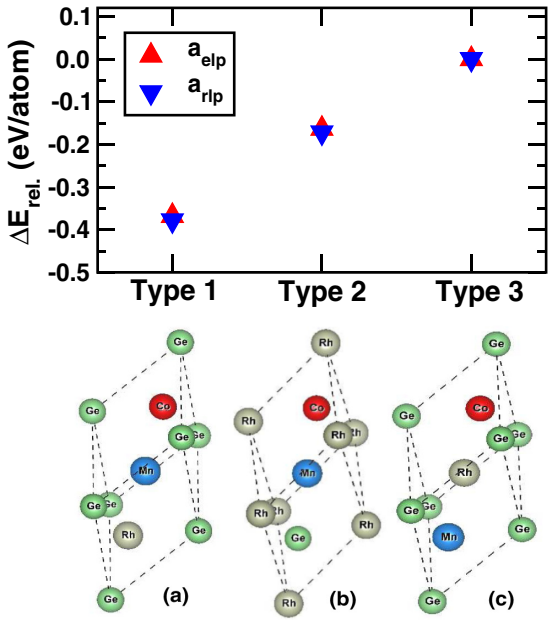

FIG. 1. Relative energy ($\Delta E_{\rm rel}$) of different nondegenerate atomic configurations with respect to Type3 configuration, calculated at experimental ($a_{\rm elp}$) and relaxed ($a_{\rm rlp}$) lattice parameters. Three distinct configurations, Type1, Type2, and Type3, are shown by the primitive unit cell (a), (b), and (c), respectively, and are detailed in the text.

stable structure, Type3, is formed when Co occupies at 4*d*, Rh at 4*b*, Mn at 4*c*, and Ge at 4*a* Wyckoff sites, respectively. All the theoretical calculations have been performed by choosing Type1 configuration.

B. Electronic structure, magnetic, and mechanical properties

In this section, spin polarized electronic structure, magnetic properties, and the mechanical stability of CRMG alloy are presented using *ab initio* simulations. Figure 2 shows spin polarized band structure and density of states calculated at a theoretically relaxed lattice parameter ($a_{\rm rlp} = 5.92$ Å). CRMG shows an indirect band gap of 0.23 eV from $\Gamma \rightarrow X$ in the minority spin channel and finite DOS at E_F in the majority spin channel. Due to the occurrence of an extremely small state at E_F for the minority spin channel, CRMG acquires a slightly small spin polarization (99.8%) compared to the ideal one. Experimental lattice parameter ($a_{\rm elp}$) is measured to be 5.89 Å, which is not very different from that of $a_{\rm rlp}$. Calculated band structure at $a_{\rm elp}$ looks very similar to that of Fig. 2 with a band gap of 0.23 eV.

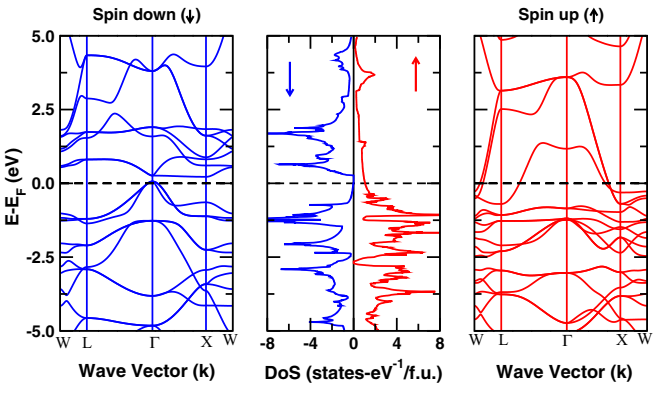

FIG. 2. Band structure and the density of states (DOS) for CRMG at $a_{\rm rlp}$. The system shows a half-metallic characteristic having a finite DOS in spin up channel at E_F and a nonzero indirect band gap [$(\Delta E_g)_\downarrow = 0.23$ eV] in the spin down channel at E_F. Dashed line represents the Fermi level (E_F).

The calculated total magnetic moment ($m_{\rm tot}$) is 4.94 μ_B/f.u. at $a_{\rm rlp}$, which follows the Slater-Pauling rule [16–19], according to which $m = (N_v - 24)\mu_B$, where N_v is the number of valence electrons per unit cell. Our experimentally measured total moment is 4.9 μ_B/f.u.. We have also calculated the Curie temperature (T_C) using the model presented in Refs. [20,21]. The calculated T_C comes out to be 915 K (917 K) with $a_{\rm elp}$ ($a_{\rm rlp}$), which compares fairly well with those measured by us (∼760 K).

We have also checked the mechanical stability of the alloy by performing lattice dynamics calculations. The linear response parameters, e.g., elastic constants (C_{ij}), are nothing but the proportionality factor of stress and strain of the crystal under applied force. Calculated values of C_{ij} for CRMG at equilibrium lattice constant ($a_{\rm rlp}$) are $C_{11} = 259.83$, $C_{12} = 167.41$, and $C_{44} = 98.00$ GPa. The condition for mechanical stability of cubic crystals, the so-called Born-Huang criteria [22], is defined as

$$C_{11} > 0, \quad C_{44} > 0, \quad C_{11} > C_{12}, \quad (C_{11} + 2C_{12}) > 0.$$

These criteria hold very well in the present case and hence CRMG is mechanically stable. The other elastic moduli such as Bulk modulus (B), shear modulus (G), Young's modulus (Y), and the anisotropy factor (A) are also calculated and are given by 198.22, 72.83, 194.65, and 2.12, respectively.

C. Pressure effect on electronic structure and mechanical stability

Due to the high value of spin polarization, the half-metallic materials are frequently used in spintronic devices in the form of thin films or multilayer. The lattice parameters of pristine bulk materials usually change when the films or multilayer are grown on appropriate substrates. As such, it is important to check the effect of lattice parameter variation (or pressure) on the electronic structure of bulk material which can give some hints for the surface properties.

Effect of hydrostatic pressure on the CRMG alloy has been investigated theoretically by reducing the value of the lattice constant from its equilibrium value. Pressure effect on electronic structure, magnetism, and mechanical properties are summarized in Tables I, II, and III, respectively. The alloy retains its half-metallic characteristics in a limited range of pressure (up to 5.70 Å, which corresponds to 30.27 GPa pressure) with variable band-gap and DOS value in the minority and majority spin channels at E_F. Below 3.2% reduction of the lattice parameter (i.e., <5.70 Å) with respect to $a_{\rm elp}$, DOS in the minority spin channel grows tremendously and resulted in a complete suppression of the band gap and consequently a phase transition from half-metallic to metallic state (Table I).

TABLE I. Effect of pressure on the electronic properties of CRMG. Up to 5.70 Å (pressure of 30.27 GPa), the system retains its half-metallic characteristics with the variable band gap $[(\Delta E_g)_\downarrow]$ and DOS $[n_\uparrow(E_F)$ and $n_\downarrow(E_F)]$. A phase transition from half-metallic (HM) to metallic occurs below 5.70 Å (i.e., above 30.27 GPa). Band gap, DOS, and pressure are measured in eV, states/eV f.u. and GPa, respectively.

a (Å)	Pressure	$n_\uparrow(E_F)$	$n_\downarrow(E_F)$	$(\Delta E_g)_\downarrow$	Nature
5.00	327.08	1.40	2.10	No gap	Metallic
5.10	252.96	1.13	1.92	No gap	Metallic
5.20	193.39	0.92	1.86	No gap	Metallic
5.30	145.24	0.90	1.86	No gap	Metallic
5.40	106.54	0.87	1.48	No gap	Metallic
5.50	75.32	0.87	1.04	No gap	Metallic
5.60	50.30	0.89	0.49	No gap	Metallic
5.70	30.27	0.94	0.00	0.32	HM
5.80	14.57	1.00	0.00	0.28	HM
5.85	8.09	1.03	0.00	0.26	HM
5.89 ($a_{\rm elp}$)	3.49	1.05	0.00	0.25	HM
5.92 ($a_{\rm rlp}$)	0.00	1.07	0.00	0.23	HM
6.00	−6.86	1.12	0.05	No gap	Metallic

We have simulated various magnetic configurations involving ferromagnetic, antiferromagnetic, and ferrimagnetic arrangements. Of all these, the ferromagnetic configuration is found to be energetically the most favorable configuration and hence the magnetic ground state. There is no magnetic transition seen in the considered range of pressure and the system retains its ferromagnetic characteristics, but with decreasing magnitude in $m_{\rm tot}$ (Table II). Thus the system is robust against magnetic transition.

Table III summarizes the effect of pressure on the mechanical properties of the CRMG alloy. Elastic constant C_{ij} and various elastic moduli are affected very significantly. As the pressure increases, the elastic moduli B, G, Y, and A reduces. Up to 5.40 Å (i.e., 106.5 GPa), CRMG satisfies the Born-Huang criteria but below 5.40 Å, the alloy becomes mechanically unstable.

TABLE II. Pressure effect on the atom projected and total magnetic moment (in Bohr magneton units) of CRMG. All the constituent transition metal elements are ferromagnetically aligned. Notably, the system retains its ferromagnetic characteristics throughout the pressure range, i.e., there is no magnetic phase transition.

a (Å)	$m_{\rm Co}$	$m_{\rm Rh}$	$m_{\rm Mn}$	$m_{\rm Ge}$	$m_{\rm tot}$
5.00	0.69	0.38	2.44	0.02	3.52
5.10	0.76	0.39	2.65	0.01	3.80
5.20	0.87	0.42	2.81	0.01	4.12
5.30	0.97	0.45	2.95	0.01	4.38
5.40	1.06	0.48	3.06	0.01	4.60
5.50	1.14	0.49	3.15	0.00	4.77
5.60	1.20	0.50	3.21	−0.01	4.89
5.70	1.20	0.47	3.26	−0.01	4.91
5.80	1.20	0.44	3.31	−0.02	4.92
5.85	1.20	0.42	3.33	−0.03	4.93
5.89 ($a_{\rm elp}$)	1.20	0.41	3.36	−0.03	4.93
5.92 ($a_{\rm rlp}$)	1.20	0.39	3.37	−0.03	4.94
6.00	1.20	0.37	3.42	−0.04	4.95

D. X-ray diffraction

Figure 3 shows the Rietveld refinement of the room temperature XRD pattern using Fullprof suite. It is clear from the pattern that the alloy CRMG exhibits a cubic structure. The quaternary Heusler alloys exhibit LiMgPdSn-type structure whose primitive cell contains four atoms on the Wyckoff positions 4a, 4b, 4c, and 4d. Out of various possibilities for the occupancy of four atoms at different sites, only three atomic configurations turn out to be energetically distinct for this structure [10,23]. Due to the underlying symmetry of $F\bar{4}3m$ (no. 216) space group, interchange of atoms between 4a and 4b or 4c and 4d Wyckoff positions does not change the overall symmetry and hence the total energy of the compound. The presence of superlattice reflections in the XRD pattern confirms CRMG alloy to crystallize in cubic Heusler structure. The lattice parameter was found to be 5.89 Å, which compares fairly well with theory ($a_{\rm rlp} = 5.92$ Å). The best fit of the observed intensities was obtained when Co, Mn, Rh, and Ge atoms were assigned the Wyckoff positions 4d, 4b, 4c, and 4a, respectively, which corresponds to a Type1 structure (Fig. 1). The measured crystal structure of CRMG alloy is shown in Fig. 4. The superlattice reflections are not very intense, which can be due to some disorder in the system. In CRMG, X(Co), Y(Mn), and Z(Ge) atoms are from the same period and their atomic scattering factors are nearly identical. In such cases, it is difficult to find out the extent of disorder using XRD. EXAFS is helpful in determining the short range chemical environment around the atoms. Thus, to further probe the local surroundings of Co, Ge, and Mn site, EXAFS measurements have been performed on the CRMG alloy, as discussed later. The electronic densities of the constituent elements at different vertical cuts are shown in Figs. 5(a)–5(d), which is generated from the XRD refinement using GFourier program in Fullprof suite. Figure 5(c) and Fig. 5(d) clearly suggest that most of the charge is distributed around Rh site. Co and Mn are surrounded by intermediate charge, while Ge has a charge density which is less than that of Rh but greater than that of Co and Mn atomic sites. Thus the position of a heavier element in the unit cell is reflected by the most dense electron density contour.

E. EXAFS analysis

Figure 6 shows the normalized EXAFS spectra of (a) Co, (b) Mn, and (c) Ge for CRMG alloy. The insets of (a) and (b) show the XANES (x-ray absorption near edge structures) spectrum of CRMG at Co and Mn K edge (red line). We have checked the possibility of oxidation of the samples by comparing the XANES spectra of the samples with that of standard metal foils and commercial powders of respective oxides. The spectra of pure metal foil reference is shown by black line in the insets. We found that the edge positions and the XANES spectra of CRMG sample agree fairly well with those of the pure metal foils and do not resemble that of the oxides, thus ruling out the presence of oxides. In order to take care of the oscillations in the absorption spectra, the absorption

TABLE III. Effect of pressure on elastic constants (C_{ij}), bulk modulus (B), shear modulus (G), Young's modulus (Y), and anisotropy factor (A) for CRMG. The alloy is mechanically stable up to 5.40 Å, satisfying Born-Huang criteria. Any further decrease in a (increase in pressure) leads to instability. The symbol, ✓(X), represents whether the Born-Huang criteria is satisfied or not. All the elastic parameters are in GPa units.

a (Å)	C_{11}	C_{12}	C_{44}	B	G	Y	A	Born-Huang criteria
5.00	939.74	1043.46	480.81	1008.88	−215.75	−696.94	−9.27	X
5.10	821.35	899.80	418.18	873.65	−113.98	−357.49	−10.66	X
5.20	695.08	754.68	360.70	734.81	−60.94	−188.02	−12.10	X
5.30	612.80	613.87	309.33	613.51	66.25	191.85	−578.19	X
5.40	561.04	494.75	264.21	516.85	118.96	331.46	7.97	✓
5.50	513.71	399.18	225.00	437.36	131.85	359.43	3.93	✓
5.60	456.75	320.94	189.77	366.21	126.70	340.79	2.79	✓
5.70	392.69	263.83	156.95	306.78	110.51	295.99	2.44	✓
5.80	327.07	215.85	128.44	252.92	92.33	246.93	2.31	✓
5.85	298.53	195.20	115.58	229.64	84.12	224.91	2.24	✓
5.89 (a_{elp})	277.01	179.72	105.88	212.15	77.89	208.20	2.18	✓
5.92 (a_{rlp})	259.83	167.41	98.00	198.22	72.83	194.65	2.12	✓
6.00	224.37	142.13	81.56	169.54	62.22	166.32	1.98	✓

function $\chi(E)$ is calculated as follows [24]:

$$\chi(E) = \frac{\mu(E) - \mu(E_0)}{\Delta\mu(E_0)}. \quad (3)$$

Here E_0 is absorption edge energy, $\Delta\mu(E_0)$ is the bare atom background, and $\mu(E)$ is the step in value at the absorption edge. The k-dependent absorption coefficient $\chi(k)$ is then calculated using the relation

$$k = \sqrt{\frac{2m(E - E_0)}{\hbar^2}}, \quad (4)$$

where m is the electronic mass. $\chi(k)$ is then weighted by k^3 to amplify the oscillation at high k. The $k^3 * \chi(k)$ spectra for Co, Mn, and Ge k edge are shown in Fig. 7. The $k^3\chi(k)$ functions are also Fourier transformed in the R space to generate the $\chi(R)$ spectra in terms of the real distances from the center of the absorbing atom. The set of EXAFS data analysis programs available within the IFEFFIT software package has been used for final data analysis [25]. This includes background reduction and Fourier transform to derive the $\chi(R)$ versus R spectra from the absorption spectra (using ATHENA software), generation of the theoretical EXAFS spectra starting from an assumed crystallographic structure, and finally fitting of experimental data with the theoretical spectra using ARTEMIS software.

The $\chi(R)$ versus R spectra generated (Fourier transform range is $k = 3.0$–10.0 Å^{-1} for the CRMG sample) using the methodology described above are shown in Fig. 8 for CRMG measured at Co, Mn, and Ge K edge. The fitting strategy adopted here was to simultaneously fit multiple data sets with multiple edges [26,27]. Co, Mn, and Ge K edges are fitted simultaneously with common fitting parameters. This fitting reduces the number of independent parameters below the Nyquist criteria and enhances the statistical significance of the fitting model. The goodness of fit has been determined by

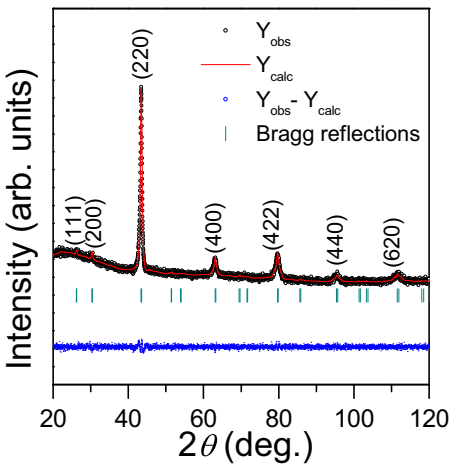

FIG. 3. Rietveld refined XRD pattern of CRMG alloy. Y_{obs} and Y_{calc} are the observed and calculated scattering intensities.

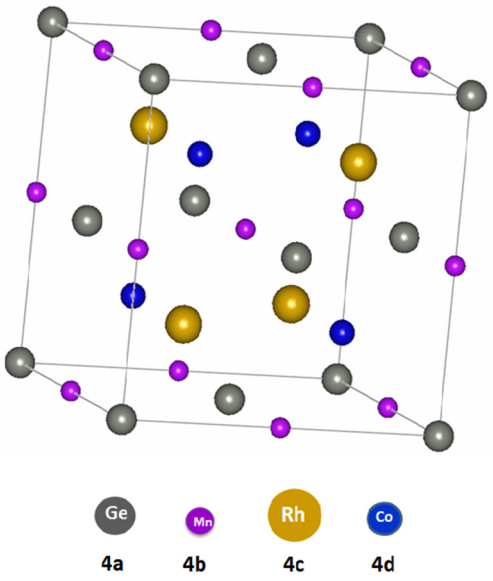

FIG. 4. Measured crystal structure of CRMG alloy.

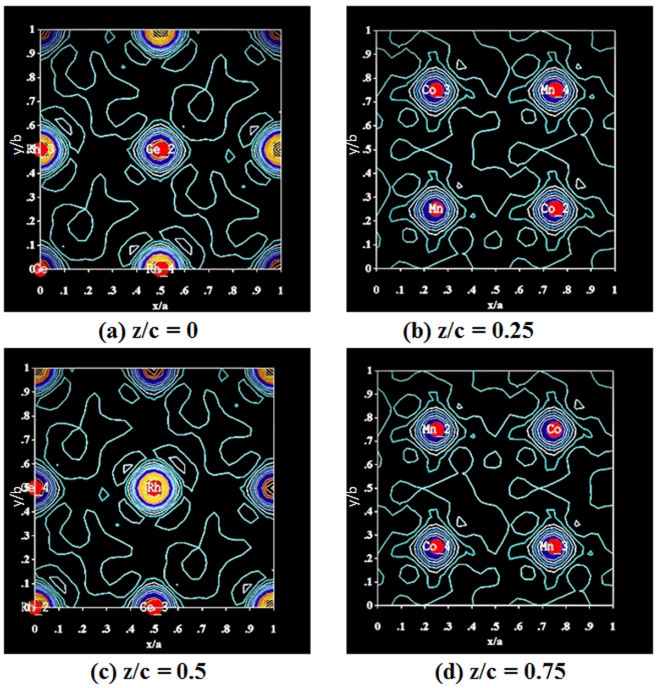

FIG. 5. Electronic density of individual atoms in the unit cell of CRMG alloy at (a) $z/c = 0$, (b) $z/c = 0.25$, (c) $z/c = 0.5$, and (d) $z/c = 0.75$.

the value of the R_{factor} defined by

$$R_{\text{factor}} = \sum_i \frac{[\text{Im}(\chi_{\text{dat}}(r_i) - \chi_{\text{th}}(r_i))]^2 + [\text{Re}(\chi_{\text{dat}}(r_i) - \chi_{\text{th}}(r_i))]^2}{[\text{Im}(\chi_{\text{dat}}(r_i))]^2 + [\text{Re}(\chi_{\text{dat}}(r_i))]^2}, \tag{5}$$

where χ_{dat} and χ_{th} refer to the experimental and theoretical $\chi(r)$ values, respectively, and Re and Im refer to the real and imaginary parts of the respective quantities. In addition to the single scattering paths, multiple scattering paths are also used for the fitting purpose.

The structural parameters (atomic coordination and lattice parameters) of CRMG used for simulation of theoretical EXAFS spectra of the sample have been obtained from XRD results. The best fitted $\chi(R)$ versus R spectra (fitting range $R = 1.2$–5.0 Å) of the sample are shown in Fig. 8 along with the experimental data for the measurements carried out at Co, Mn, and Ge K edges. The bond distances, coordination numbers (including scattering amplitudes), and disorder (Debye-Waller) factors (σ^2), which give the mean square fluctuations in the distances, have been used as fitting parameters. All the three spectra are fitted without site antisite disorder. Thus the structural characterization of the CRMG performed using EXAFS analysis reveals a well ordered structure for CRMG (no antisite disorder). All the relevant fitting parameters are shown in Table IV.

In the Fourier transformed EXAFS spectrum of Co K edge [Fig. 8(a)], the main peak near 2.1 Å has contribution from Co-Ge (2.40 Å), Co-Rh (2.40 Å), and Co-Mn (2.92 Å) paths. The small peak around 3.5 Å at Co K-edge spectrum is the contribution of Co-Co (4.05 Å) coordination and a small

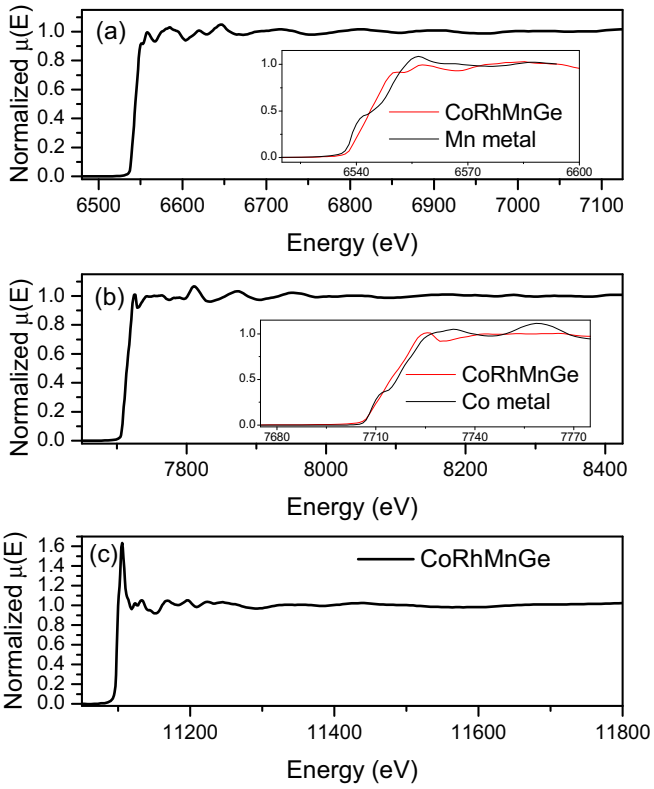

FIG. 6. Normalized EXAFS spectra of (a) Co, (b) Mn, and (c) Ge of CRMG sample. The insets of (a) and (b) show the XANES spectrum of CRMG at Co and Mn K edge (red line) along with the corresponding metal foil reference (black line).

contribution of higher bond length paths. The third peak at 4.25 Å is the contribution from Co-Ge (4.60 Å) and Co-Rh (4.60 Å) coordination shells with multiple scattering paths. The use of multiple scattering paths does not include any further independent parameters as all the multiple scattering parameters are defined in terms of single scattering path

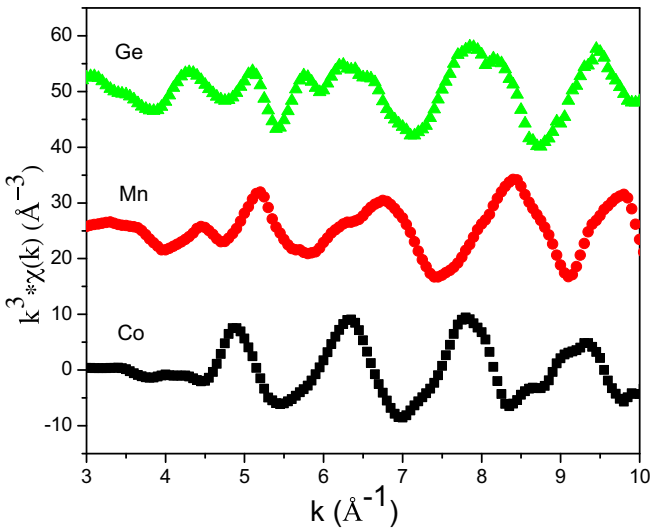

FIG. 7. $k^3 * \chi(K)$ vs k spectra for Co, Mn, and Ge of k edge of CRMG.

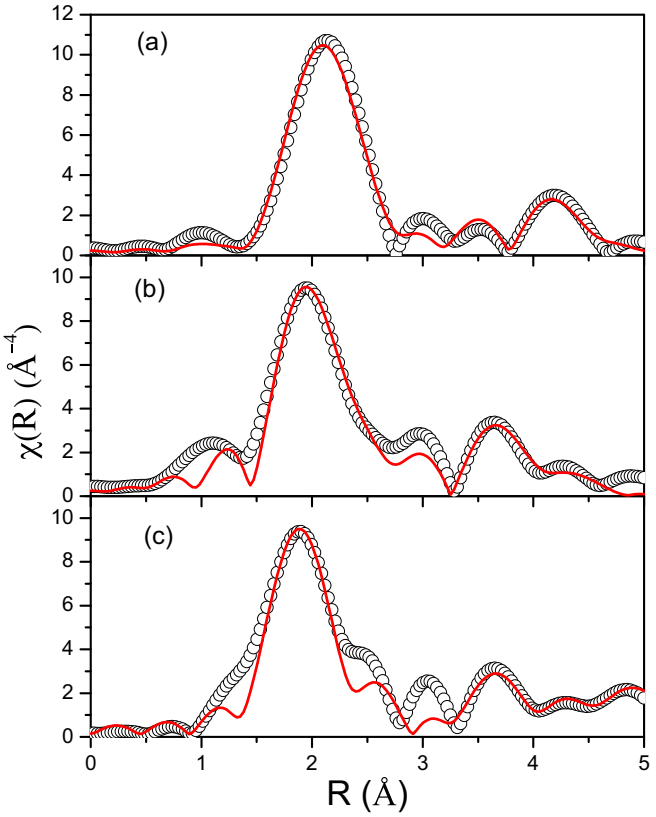

FIG. 8. Fourier transformed EXAFS spectra $\chi(R)$ of CRMG at (a) Co, (b) Mn, and (c) Ge K edge (scatter points) and theoretical fit (red solid line).

parameters [27]. In the case of Ge K edge [Fig. 8(c)], the first peak has the contribution from Ge-Co (2.39 Å), Ge-Mn (2.39 Å), and Ge-Rh (2.92 Å) paths. The peak at 3 Å could not be fitted well as there is no coordination shell present at this distance. The peak at 3.6 Å is the contribution from Ge-Ge (4.11 Å) path. The double peak between 4 Å and 5 Å is fitted with Ge-Co (4.89 Å), Ge-Mn (4.89 Å), and multiple scattering paths. Similarly, in the case of Mn K edge [Fig. 8(b)] the first peak has the contribution from Mn-Ge (2.40 Å), Mn-Rh (2.40 Å), and Mn-Co (2.89 Å). The region between 3.5 Å and 4.5 Å is fitted with Mn-Mn, Mn-Ge, and Mn-Rh coordination shells with multiple scattering paths.

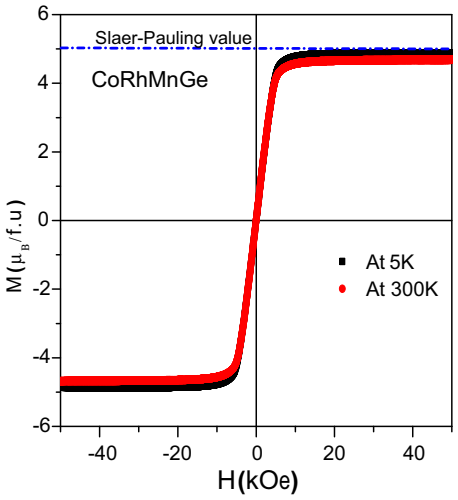

FIG. 9. Magnetization curves for CRMG alloy at 5 K and 300 K.

F. Magnetic properties

Figure 9 shows the isothermal magnetization curves for the CRMG alloy at 5 K and 300 K. Negligibly small hysteresis shows the soft magnetic nature of the alloy, as also observed in other [3,16] similar alloys systems. To be precise, the hysteresis observed here is associated with a small coercive field of ∼30 Oe and a finite but small remanent magnetization (∼0.025 μ_B/f.u.). Given the polycrystalline nature of the compound, it is however difficult to determine the hard and/or easy axes in the present case. The saturation magnetization values (M_s) at 5 K and 300 K were found to be 4.9 μ_B/f.u. and 4.7 μ_B/f.u., respectively. The obtained M_s value (at 5 K) is in close agreement with those expected from the Slater-Pauling rule (5 μ_B/f.u.), which gives another indication of the half-metallic nature of this alloy.

Figure 10 shows the temperature dependence of the magnetization at a constant field of 100 Oe. The Curie temperature (T_c) is found to be ∼760 K.

G. Transport properties

Figure 11 shows the measured and fitted temperature dependence of resistivity for CRMG at 0 kOe. The inset (b) represents the ρ versus T at two different fields 0 kOe and 50 kOe, indicating insignificant dependence of ρ on the field.

TABLE IV. Bond length (R), coordination number (N), and Debye-Waller or disorder factor (σ^2) obtained by EXAFS fitting for CRMG at Co, Mn, and Ge K edge.

Co edge				Mn edge				Ge edge			
Path	R (Å)	N	σ^2	Path	R (Å)	N	σ^2	Path	R (Å)	N	σ^2
Co-Ge	2.40 ± 0.01	4	0.0085 ± 0.001	**Mn-Ge**	2.40 ± 0.01	4	0.001 ± 0.0008	**Ge-Co**	2.39 ± 0.01	4	0.02 ± 0.002
Co-Rh	2.40 ± 0.01	4	0.035 ± 0.002	**Mn-Rh**	2.40 ± 0.01	4	0.001 ± 0.0008	**Ge-Mn**	2.39 ± 0.01	4	0.0057 ± 0.001
Co-Mn	2.92 ± 0.01	6	0.0142 ± 0.001	**Mn-Co**	2.89 ± 0.02	6	0.0167 ± 0.001	**Ge-Rh**	2.92 ± 0.01	6	0.0199 ± 0.0008
Co-Co	4.05 ± 0.02	12	0.0255 ± 0.0009	**Mn-Mn**	4.05 ± 0.01	12	0.0321 ± 0.001	**Ge-Ge**	4.11 ± 0.03	12	0.0128 ± 0.006
Co-Ge	4.60 ± 0.03	12	0.0098 ± 0.001	**Mn-Ge**	4.58 ± 0.02	12	0.004 ± 0.001	**Ge-Co**	4.89 ± 0.05	12	0.0039 ± 0.001
Co-Rh	4.60 ± 0.03	12	0.0077 ± 0.0007	**Mn-Rh**	4.63 ± 0.02	12	0.0043 ± 0.001	**Ge-Mn**	4.89 ± 0.05	12	0.0026 ± 0.001

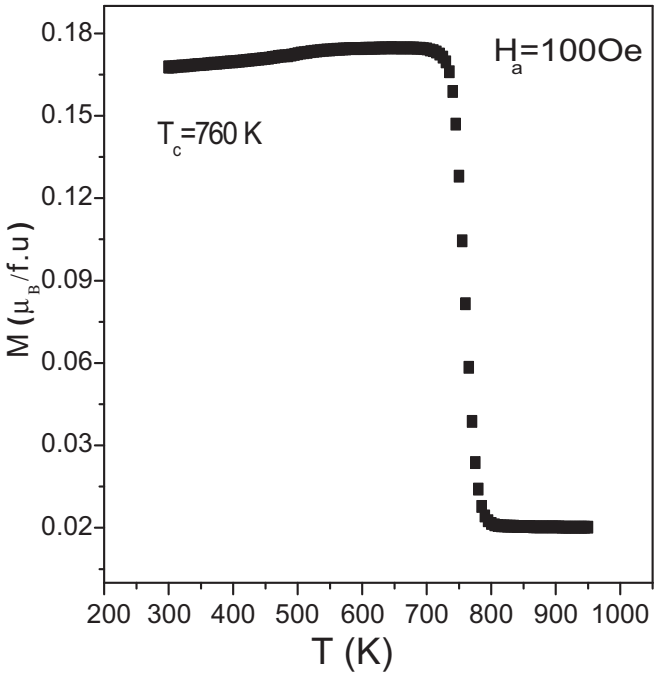

FIG. 10. Temperature dependence of magnetization at 100 Oe. T_c is calculated from the minima of the first order derivative of M vs T curve.

To closely investigate the half-metallic nature of CRMG, we have used two different functions for fitting the zero field resistivity curve. The residual resistivity is found to be 48.16 $\mu\Omega$ cm. In the first approach, we have fitted the resistivity data to a general power law,

$$\rho(T) = \rho_0 + \rho_n T^n,$$

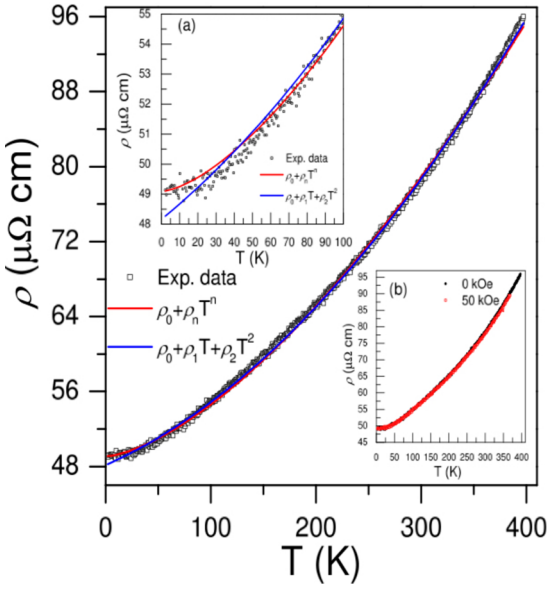

FIG. 11. Temperature dependence of electrical resistivity(ρ) for CRMG at zero field. The raw data is fitted with two functions, a general power law and a quadratic fit. Inset (a) shows a closer look of the ρ curve between 0 and 100 K. Inset (b) shows ρ vs T at 0 and 50 kOe.

where ρ_0 is the residual resistivity. The value of n, when fitted in the temperature range 2–400 K is found to be 1.53. In previous reports on Heusler compounds, several authors have obtained different power (n) values depending on the temperature range considered. However, the value of n is compound specific. For example, $n = 1.55$ was obtained for NiMnSb for $120 < T < 300$ K [28], which was attributed to the resistivity of spin fluctuation magnets and for Co_2FeGa [29] n was found to be 1.31 for $60 < T < 250$ K. In the present report for CoRhMnGe, the resistivity is found to follow $T^{1.53}$ power law within $2 < T < 400$ K. A similar $T^{3/2}$ dependence is also seen in half-metallic CoRuFeGe [30] and Co_2MnGe [31] systems. In general, the observed $T^{3/2}$ dependence of resistivity may be ascribed to the incoherent electron-magnon scattering as reported earlier [32].

In the second approach, the resistivity curve was fitted using the equation

$$\rho(T) = \rho_0 + \rho_{\text{phonon}} + \rho_{\text{magnon}} = \rho_0 + \rho_1 T + \rho_2 T^2, \quad (6)$$

where ρ_1 and ρ_2 are arbitrary constants, ρ_0 is the residual resistivity which originates from the scattering of conduction electrons by the lattice defects, impurities, etc., and ρ_{phonon} and ρ_{magnon} arise due to scattering of phonons and magnons, respectively. With the quadratic temperature dependence, the curve fits well for temperature $T > 35$ K, as shown in the inset (a) of Fig. 11. At low temperatures, however, the electrical resistivity is found to be almost independent of temperature (2–35 K). Similar behavior was also observed for other half-metallic ferromagnets like CoRuFeSi [30] and Co_2FeSi [33]. The results of the fitting are given in Table V. It can be seen that the dominant contribution is from the electron-phonon scattering (T dependence).

In a half-metallic ferromagnet, the states at E_F are completely spin-polarized, and hence spin-flip scattering is not possible [34,35] due to absence of electrons in the minority band gap at E_F. Thus, for a half-metallic ferromagnet, T^2 term is expected to be absent in the resistivity. The insignificant contribution of T^2 term in the resistivity data for the CRMG alloy indirectly supports the half-metallic nature.

V. SUMMARY AND CONCLUSION

In summary, we have studied the structural, electronic, magnetic, and transport properties of equiatomic quaternary Heusler alloy CoRhMnGe by means of theory and experiment. Experimentally prepared alloy crystallizes in Y-type structure with almost no signature of intrinsic disorder. *Ab initio* simulation confirms the stability of the measured crystal structure. It also confirms the half-metallic nature of the alloy (leading to high spin polarization), which is supported by the experimentally observed (almost) integer moment ($\sim 5.0\mu_B$) at 5 K. In addition, measured electrical resistivity also indirectly supports the half-metallic behavior in the alloy. Pressure studies reveal that the half-metallic nature of CRMG remains robust within a limited range of pressure (up to 30.27 GPa), beyond which it becomes metallic. There is, however, no evidence of magnetic phase transition. Electronic energy and lattice dynamics calculations show that the system is chemically as well as mechanically stable. Summarizing all these properties along with high spin polarization and

TABLE V. Fitting parameters for zero field electrical resistivity vs T for CRMG alloy. Two different fitting procedures involve a general power law and a quadratic fit. Residual resistivity (ρ_0) in both cases is the same, i.e., $\rho_0 = 48.16\ \mu\Omega$.

$\rho(T) = \rho_0 + \rho_n T^n$	$\rho_n = 0.0047(1)\ \mu\Omega\,\mathrm{cm\,K^{-n}}$	$n = 1.535(4)$
$\rho(T) = \rho_0 + \rho_1 T + \rho_2 T^2$	$\rho_1 = 0.0496(4)\ \mu\Omega\,\mathrm{cm\,K^{-1}}$	$\rho_2 = [1.742(1)] \times 10^{-4}\ \mu\Omega\,\mathrm{cm\,K^{-2}}$

relatively large value of T_C (~760 K) makes CRMG a potential candidate for spintronic applications.

ACKNOWLEDGMENTS

D.R. would like to thank Council of Scientific and Industrial Research (CSIR), India for providing Junior Research Fellowship support and Dr. S. Shanmukharao Samatham for help in resistivity measurement. Enamullah acknowledges Indian Institute of Technology Bombay for necessary funding to support this research through an Institute Post Doctoral Fellowship. A.A. acknowledges DST-SERB (Grant No. SB/FTP/PS-153/2013) for funding to support this research.

D.R. and E. contributed equally to this work.

[1] C. Felser, G. Fecher, and B. Balke, Angew. Chem., Int. Ed. Engl. **46**, 668 (2007).
[2] R. A. de Groot, F. M. Mueller, P. G. van Engen, and K. H. J. Buschow, Phys. Rev. Lett. **50**, 2024 (1983).
[3] L. Bainsla and K. G. Suresh, Appl. Phys. Rev. **3**, 031101 (2016).
[4] T. Graf, C. Felser, and S. S. Parkin, Prog. Solid State Chem. **39**, 1 (2011).
[5] L. Bainsla, K. G. Suresh, A. K. Nigam, M. Manivel Raja, B. S. D. C. S. Varaprasad, Y. K. Takahashi, and K. Hono, J. Appl. Phys. **116**, 203902 (2014).
[6] L. Bainsla, A. I. Mallick, M. M. Raja, A. K. Nigam, B. S. D. C. S. Varaprasad, Y. K. Takahashi, A. Alam, K. G. Suresh, and K. Hono, Phys. Rev. B **91**, 104408 (2015).
[7] T. M. Nakatani, A. Rajanikanth, Z. Gercsi, Y. K. Takahashi, K. Inomata, and K. Hono, J. Appl. Phys. **102**, 033916 (2007).
[8] A. Rajanikanth, Y. K. Takahashi, and K. Hono, J. Appl. Phys. **101**, 023901 (2007).
[9] M. Julliere, Phys. Lett. A **54**, 225 (1975).
[10] V. Alijani, J. Winterlik, G. H. Fecher, S. S. Naghavi, S. Chadov, T. Gruhn, and C. Felser, J. Phys.: Condens. Matter **24**, 046001 (2012).
[11] https://www.ill.eu/sites/fullprof/php/tutorials.html
[12] A. K. Poswal, A. Agrawal, A. K. Yadav, C. Nayak, S. Basu, S. R. Kane, C. K. Garg, D. Bhattachryya, S. N. Jha, and N. K. Sahoo, AIP Conf. Proc. **1591**, 649 (2014).
[13] S. Basu, C. Nayak, A. K. Yadav, A. Agrawal, A. K. Poswal, D. Bhattacharyya, S. N. Jha, and N. K. Sahoo, J. Phys. Conf. Ser. **493**, 012032 (2014).
[14] G. Kresse and J. Furthmüller, Phys. Rev. B **54**, 11169 (1996).
[15] G. Kresse and D. Joubert, Phys. Rev. B **59**, 1758 (1999).
[16] V. Alijani, J. Winterlik, G. H. Fecher, S. S. Naghavi, and C. Felser, Phys. Rev. B **83**, 184428 (2011).
[17] I. Galanakis, P. H. Dederichs, and N. Papanikolaou, Phys. Rev. B **66**, 174429 (2002).
[18] J. C. Slater, Phys. Rev. **49**, 931 (1936).
[19] L. Pauling, Phys. Rev. **54**, 899 (1938).
[20] A. Alam, B. Kraczek, and D. D. Johnson, Phys. Rev. B **82**, 024435 (2010).
[21] A. Alam, M. Khan, R. W. McCallum, and D. D. Johnson, Appl. Phys. Lett. **102**, 042402 (2013).
[22] M. Born and K. Huang, *Dynamical Theory of Crystal Lattices* (Oxford University Press, Oxford, UK, 1954).
[23] Enamullah, Y. Venkateswara, S. Gupta, M. R. Varma, P. Singh, K. G. Suresh, and A. Alam, Phys. Rev. B **92**, 224413 (2015).
[24] *X-Ray Absorption: Principles, Applications Techniques of EXAFS, SEXAFS and XANES*, edited by D. Konigsberger and R. Prince (Wiley, New York, 1988).
[25] M. Newville, B. Ravel, D. Haskel, J. Rehr, E. Stern, and Y. Yacoby, Phys. B (Amsterdam, Neth.) **208**, 154 (1995).
[26] L. Bainsla, A. Yadav, Y. Venkateswara, S. Jha, D. Bhattacharyya, and K. Suresh, J. Alloys Compd. **651**, 509 (2015).
[27] B. Ravel, M. P. Raphael, V. G. Harris, and Q. Huang, Phys. Rev. B **65**, 184431 (2002).
[28] S. Gardelis, J. Androulakis, P. Migiakis, J. Giapintzakis, S. K. Clowes, Y. Bugoslavsky, W. R. Branford, Y. Miyoshi, and L. F. Cohen, J. Appl. Phys. **95**, 8063 (2004).
[29] M. Zhang, E. Brck, F. R. de Boer, Z. Li, and G. Wu, J. Phys. D: Appl. Phys. **37**, 2049 (2004).
[30] L. Bainsla, M. M. Raja, A. Nigam, and K. Suresh, J. Alloys Compd. **651**, 631 (2015).
[31] T. Ambrose, J. J. Krebs, and G. A. Prinz, Appl. Phys. Lett. **76**, 3280 (2000).
[32] F. Goedsche and A. Richter, Phys. Status Solidi B **96**, 279 (1979).
[33] D. Bombor, C. G. F. Blum, O. Volkonskiy, S. Rodan, S. Wurmehl, C. Hess, and B. Büchner, Phys. Rev. Lett. **110**, 066601 (2013).
[34] M. J. Otto, R. A. M. van Woerden, P. J. van der Valk, J. Wijngaard, C. F. van Bruggen, and C. Haas, J. Phys.: Condens. Matter **1**, 2351 (1989).
[35] N. Kubo and K. Ohata, J. Phys. Soc. Jpn. **33**, 21 (1972).